Iron mineral dissolution during permafrost thaw releases associated organic carbon

Monique S. Patzner[1], Carsten W. Mueller[2], Miroslava Malusova[1], Verena Nikeleit[1], Thomas Scholten[3], Carmen Hoeschen[2], James M. Byrne[1], Thomas Borch[4], Andreas Kappler[1] & Casey Bryce[1]*

[1] Geomicrobiology, Center for Applied Geosciences, University of Tuebingen, Tuebingen, Germany.

[2] Chair of Soil Science, Technical University Muenchen, Freising, Germany.

[3] Chair of Soil Science and Geomorphology, University of Tuebingen, 72070 Germany.

[4] Department of Soil & Crop Sciences and Department of Chemistry, Colorado State University, Fort Collins, US.

*Corresponding Author: Casey Bryce **Email:** casey.bryce@uni-tuebingen.de

Classification

PHYSICAL SCIENCES: Environmental Sciences.

Keywords

iron carbon associations, iron reduction, Abisko, Arctic, peatland

Author Contributions

The original hypothesis was formulated by C.B and A.K. M.P, C.B and A.K designed the project, interpreted the data and wrote the manuscript. M.P, C.B and M.M collected the samples. M.P gathered the data presented in the main text. Supporting information from the 2017 campaign was collected by V.N, M.M and C.B. T.B conducted the synchrotron analysis and contributed to the data analysis and interpretation. C. H. and C.W.M, together with M.P, collected, analyzed and interpreted the nanoSIMS data. J.B and M.P conducted the SEM analyses. T.S contributed to project design and data interpretation. All authors contributed to the preparation of the manuscript.

This PDF file includes:

Main Text

Figures 1 to 4

Figures S1 to S9

Tables S1

1 **Abstract**

2 The release of vast amounts of organic carbon during thawing of high-latitude permafrost is an

3 emerging issue of global concern, yet it is unclear what controls the amount of this released

4 carbon that will be subsequently metabolized and emitted as greenhouse gases. It has been

5 shown that reactive soil minerals, specifically iron (oxyhydr)oxides, can trap approximately

6 20% of total organic carbon in soils overlying intact permafrost (1), and may limit carbon

7 mobilization and degradation as is observed in other environments. However, the stability of

8 iron-bearing minerals and thus their capacity to prevent carbon mobilization during permafrost

9 thaw is entirely unknown. We have followed the dynamic interactions between iron and carbon

10 across a thaw gradient in Abisko (Sweden), where wetlands are expanding rapidly due to

11 permafrost thaw. Using both bulk (selective extractions, EXAFS) and nanoscale analysis

12 (correlative SEM and nanoSIMS), we found that a maximum of 19.4±0.7% of the total soil

13 organic carbon is associated with reactive iron minerals in palsas underlain by intact

14 permafrost. However, the soil becomes water-logged and oxygen limited when palsas

15 collapse, resulting in reducing conditions, an increase in abundance of Fe(III)-reducing

16 bacteria, and a mobilization of both iron and carbon along the thaw gradient. Our results show

17 that waterlogging and anoxia associated with permafrost thaw effectively destroys this "rusty

18 carbon sink" (2) in permafrost soils.

19 **Significance Statement**

20 There is significant concern that warming-induced permafrost collapse will release yet more

21 greenhouse gases like CO_2 and CH_4. It has been shown that reactive iron minerals in soils can

22 protect carbon from degradation in intact permafrost regions, providing a so-called "rusty

23 carbon sink" and limiting emissions. However, our results demonstrate that reactive iron

24 minerals only stabilize carbon when permafrost is intact. When permafrost thaws, microbially-

25 driven mineral dissolution releases trapped carbon. We show that the "rusty carbon sink" is

26 vulnerable to thaw-induced changes in redox state, and identify an over-looked source of

27 organic carbon to thaw lakes and wetlands in permafrost regions. Release of mineral-

28 associated carbon may have consequences for greenhouse gas emissions that are

29 unaccounted for in current predictions.

30

31 **Main Text**

32 **Introduction**

33   Permafrost soils store almost twice as much carbon as is currently present in the

34 atmosphere (3, 4), which is at risk of being released as greenhouse gases (i.e., CO_2 or CH_4)

35 during thawing. Release of greenhouse gases from permafrost soils provides a feedback which

36 will likely lead to faster warming than predicted from anthropogenic activities alone (5). This is

37 especially concerning considering that high latitude regions are experiencing significantly

38 higher rates of warming than the global average (0.6°C per decade in Northern Hemisphere,

39 1.35°C per decade in the Arctic specifically) (6, 7). However, the extent of greenhouse gas

40 emissions from thawing permafrost remains unpredictable due to knowledge gaps related to

41 controls on the fate of carbon in permafrost soils. Indeed, it has been suggested that the

42 permafrost-carbon feedback is the most important carbon-cycle feedback missing from climate

43 models and one of the greatest uncertainties in future climate predictions (8).

44   The mobility, lability and bioavailability of organic carbon in the environment is determined

45 by a number of interconnected physico-biogeochemical parameters and processes. One such

46 parameter is the presence of reactive iron minerals (defined here as iron minerals that are

47 reductively dissolved by the chemical reductant sodium dithionite, e.g. ferrihydrite or goethite).

48 These minerals are known to sorb and co-precipitate organic carbon (9) and are thought to

49 significantly influence long-term carbon storage in numerous environments (10-13). For

50 example, approximately 20% of total organic carbon in marine sediments is associated with

51 such reactive iron minerals (12).

52   However, the inventory of reactive iron minerals in natural systems is very dynamic as they

53 precipitate and dissolve as a response to changing redox conditions. When mineral dissolution

3

54 occurs, carbon mobilization, increased carbon lability/bioavailability and increased gaseous

55 carbon loss as CO_2 and CH_4 follows (catalyzed by heterotrophic and methanogenic

56 microorganisms) (14-18). Despite the importance of iron minerals for carbon storage, we have

57 little empirical understanding of the presence of this "rusty carbon sink" in permafrost soils or

58 of how it will respond to changing redox conditions associated with permafrost thaw.

59   In order to address this knowledge gap, we examined peatland soils collected from three

60 different thaw stages in Stordalen mire (Abisko, Sweden). Following the classification of

61 Johansson *et al* (2006) (19) (Fig. 1), these three thaw stages are: (1) desiccating palsa

62 underlain by permafrost, (2) bog with water-logged active layer underlain by permafrost, and

63 (3) fen, completely water-logged and lacking permafrost. In the desiccating palsa area, the

64 active layer is dry and oxic. As the permafrost thaws, the raised palsas collapse and become

65 inundated, transforming to an ombrotrophic bog with a waterlogged active layer but

66 continuously frozen soil underneath. With continued thawing, the bog areas decrease and

67 minerotrophic fen areas expand with complete water saturation and thus even more reducing

68 conditions than the bog. Permafrost thaw progression through these three thaw stages is,

69 however, not necessarily linear (20).

70   We took cores from all three thaw stages and analyzed iron-carbon associations in three

71 different layers within the cores defined by geochemical stratification: (1) organic horizon, (2)

72 transition zone and (3) mineral horizon (see Methods). We analyzed the solid phase by

73 selective extractions, extended X-ray absorption fine structure (EXAFS), correlative scanning

74 electron microscopy (SEM) and nanoscale secondary ion mass spectrometry (nanoSIMS).

75 This was complemented by geochemical analysis of the porewater and quantification of Fe(III)-

76 reducing bacteria which play a major role for iron mineral reduction under anoxic conditions.

Results

Thaw increases aqueous Fe(II) and dissolved organic carbon

Along the thaw gradient, the aqueous Fe(II) concentrations in the porewater increase from average concentrations of 0.02±0.01 mM in the palsa to maximum concentrations of 1.6±0.3 mM in the fen (Fig. 2). This correlates with an increase in dissolved organic carbon (DOC) from 19.7±0.8 mg/L in the palsa to 102.1±14.1 mg/L in the fen area. In the bog porewater, acetate (0.6±0.1 mM) is measurable in deeper depths, whereas lactate (0.8±0.02 mM) is only found at 7.5 cm (Fig. 2). At the fen site, lactate and acetate are detected throughout the depth profile (0.2±0.1 mM), but an additional increase in acetate (2.3±0.01 mM), propionate (0.8±0.02 mM) and butyrate (0.2±0.01 mM) at 6.5 cm depth is observed (Fig. 2). The appearance of butyrate and propionate in the fen porewater is an indicator for ongoing microbial processes such as fermentation and methanogenesis in the more water-logged and thus more reduced fen soils. This is in line with observations from previous studies (21) that highest methane emissions occur in the fen.

The abundance of Fe(III)-reducing bacteria increases with thaw

The trend in increasing aqueous Fe(II) and DOC concentrations observed across the thaw gradient closely follows the increase in abundance of Fe(III)-reducing bacteria from 2.40×10^3 cells per g soil (lower and higher 95% confidence interval 1.46×10^3 and 3.96×10^3 cells/g, respectively) in the palsa to 3.11×10^5 cells per g soil in the fen (lower and higher 95% confidence interval 1.85×10^5, and 4.78×10^5 cells/g, respectively). This is suggestive of increased microbially-driven Fe(III) mineral dissolution along the thaw gradient (Fig. 2).

Reactive iron minerals are dissolved along the thaw gradient

In order to determine whether the observed increases in DOC were related to increased Fe(III) mineral reduction and dissolution, we quantified the amount of organic carbon associated with the reactive iron minerals along the thaw gradient by applying the citrate-dithionite iron reduction method (12, 22). This method simultaneously dissolves all reactive solid iron phases and releases the organic carbon associated with these minerals into solution. The extraction

5

104   is performed at circumneutral pH to prevent hydrolysis of organic matter as well as its

105   protonation and re-adsorption onto the remaining solid phases and thus its precipitation. A

106   control experiment was conducted at the same pH with equivalent ionic strength (sodium

107   chloride instead of the reducing agent sodium dithionite). Following Lalonde *et al* (2012), the

108   organic carbon which is released in this control is not associated with the reactive iron minerals

109   and was therefore subtracted from the amount of carbon released from the dithionite-citrate

110   extractions as previously described (12). Additionally, we performed a sodium hydroxylamine-

111   HCl extraction (pH<2) to target the poorly crystalline iron minerals, a sodium pyrophosphate

112   extraction (pH 10) to extract colloidal or OM-chelated iron, and a 6 M HCl extraction to obtain

113   the total extractable Fe of the soil layers (referred to as mg Fe(tot) per g). It should be noted

114   that the total amount of iron per dry weight in the layers is different along the thaw gradient. In

115   the following, only the data from cores Palsa A, Bog C and Fen E are discussed (see Fig. 1),

116   but observed trends are supported by further analyses conducted on cores collected at the

117   same time but stored for a longer period (Palsa B, Bog D, Fen F in Fig. 1), and on triplicate

118   cores from each thaw stage collected during a previous campaign (Figs. S1, S2, S3 and S4).

119   In the transition zone of the palsa, the reducible iron mineral fraction was 72.9 to 93.9% of the

120   total extractable iron (3.5 ± 0.1 to 9.0 ± 0.3 mg Fe(tot) per g soil; Fig. 3; see also Table S1 and

121   Fig. S5). The amount of reactive iron minerals in the transition zone then decreased to 11.1%

122   of the total extractable iron (18.7 ± 0.7 mg Fe(tot) per g soil) in the bog and to 18.3% of the

123   extractable iron (14.5 ± 0.2 mg Fe(tot) per g soil) in the fen (Fig. 3). In the mineral horizons along

124   the thaw gradient, a loss of the reactive iron minerals was also observed, likely due to more

125   reduced conditions favoring Fe(III) mineral reduction at deeper depths. Reactive iron in the

126   palsa mineral layer was 10.0 to 36.6% of the total extractable iron (8.7 ± 0.3 to 13.5 ± 0.2 mg

127   Fe(tot) per g soil) and declined to 7.5% of the total extractable iron (11.7 ± 0.8 mg Fe(tot) per g

128   soil) in the bog and 9.0 to 10.7% of the total iron (16.3 ± 0.4 to 19.01 ± 0.25 mg Fe(tot) per g soil)

129   in the fen (Fig. 3). This loss of reactive iron in the transition zone and mineral horizon was also

130   confirmed by the hydroxylamine-HCl extraction and iron speciation by EXAFS (Fig. 3). The

131 abundance of colloidal and/or OM-complexed iron (defined by sodium pyrophosphate

132 extractable iron) also decreased along the thaw gradient, giving way to an increasing relative

133 atom percent-based abundance of Fe-bearing clays. This observation is consistent with

134 increasing aluminum concentrations in the extracts (Fig. S5). The iron content in the organic

135 layer increased from almost no iron in the palsa (0.2 ± 0.02 mg Fe(tot) per g soil, all poorly

136 crystalline) to 4.7 ± 0.01 mg Fe(tot) per g soil (with 43.4% of the total extractable iron being

137 reactive iron) in the organic layer of the fen (Fig. 3). We suggest this is driven by Fe(III)

138 reduction in deeper layers leading to mobilization and upwelling of Fe(II), which might

139 precipitate again close to the water surface by oxidation of Fe(II) by O_2, which diffuses from

140 the surface, followed by precipitation as Fe(III) oxyhydroxide minerals.

141 **Dissolution of reactive iron minerals releases associated organic carbon**

142 With the decline of reactive iron minerals along the thaw gradient, the mineral-associated

143 carbon was mobilized. Carbon is primarily bound to the reactive iron phases in the transition

144 zone and the mineral horizon of the palsa, as well as in the transition zone of the bog (Fig. 4).

145 9.9 to 14.8% of the total organic carbon (312.1 ± 0.3 to 354.7 ± 0.04 mg organic carbon per g

146 soil) was released by reductive dissolution of reactive iron minerals in the palsa transition (Fig.

147 4). In the palsa mineral phase, 18.7 to 20.1% of the total organic carbon (72.7 ± 0.29 to

148 136.1 ± 0.2 mg organic carbon per g soil) was released. In the transition zone of the bog, 39.4%

149 of the total organic carbon (57.5 ± 0.4 mg organic carbon per g soil) was associated with iron

150 minerals (Fig. 4). However, it should be noted that the total amount of carbon was less in these

151 samples when compared to the palsa transition zone due to total carbon loss along the thaw

152 gradient. Highest total amounts of carbon bound by the reactive iron were therefore found in

153 the palsa transition zone with 41.8 ± 10.8 mg per g soil. This is also supported by the strong

154 spatial association of C with Fe minerals in the fine fraction of this transition zone observed by

155 nanoSIMS analysis, which was not observed in other layers along the thaw gradient (Fig. 4,

156 Fig. S8). The maximum molar ratio of organic carbon to iron of 1.0, based on the maximal

157 sorption capacity of reactive iron oxides for natural organic matter (23), was exceeded in the

158 palsa transition zone and palsa mineral horizon (9.27±2.16 OC:Fe). This suggests co-

159 precipitation and/or chelation of organic compounds which can generate structures with OC:Fe

160 ratios of 6 to 10, as shown in other studies (23), and are consistent with high sodium

161 pyrophosphate extractable iron values for these palsa layers.

Discussion

163   Carbon binding to reactive iron minerals in the palsa area is consistent with previous

164 observations in permafrost regions of the Qinghai-Tibet Plateau (1) where Fe associated

165 carbon represents, on average, 19.5±12.3% of the total soil carbon pool in the upper 30 cm of

166 permafrost soils throughout the year. Our "space for time" approach reveals, for the first time,

167 how we may expect the dynamics of this rusty carbon sink to respond to progressive climate

168 change. This study suggests that, as soon as the conditions in permafrost peatlands become

169 water-logged, the reactive iron minerals are reduced, probably by Fe(III)-reducing bacteria,

170 and the associated carbon is released into the surrounding porewater, potentially leading to

171 greenhouse gas emissions. More work is needed to elucidate the chemical nature of mobilized

172 organic carbon to determine its lability, but our data suggest that direct chelation or co-

173 precipitation of Fe-C structures play an essential role in carbon protection.

174   Our findings have far-reaching implications in understanding the carbon cycle after

175 permafrost collapse. Assuming a carbon pool of 191.29 x 10^{15} g carbon in the active layer (0-

176 30 cm depth) (3) in northern permafrost regions, we suggest that 13.39 x 10^{15} to 38.26 x 10^{15}

177 g carbon could potentially be bound to reactive iron in permafrost soils. The lower estimate

178 assumes, based on our data, an average of 7% of total organic carbon is bound to reactive

179 iron in active layers underlain by intact permafrost. The higher estimate assumes a maximum

180 of 20% of total organic carbon is bound to reactive iron, based on our data and Mu *et al* (2016)

181 (1). If this iron-bound carbon was mobilized during thaw and is bioavailable, an equivalent of

182 2 to 5% of the amount of carbon which is currently present in the atmosphere could be emitted

183 as greenhouse gases from thawing permafrost sites as a consequence of iron(III) mineral

184   reduction. It is therefore crucial to further determine the amount of carbon bound to reactive

185   iron minerals in numerous permafrost environments, and the lability/bioavailability of this

186   carbon following its release in order to better predict future greenhouse gas emissions from

187   thawing permafrost soils and improve the accuracy of existing climate models.

188   **Materials and Methods**

189   **Site description and sample collection**

190   Stordalen Mire is a peatland 10 km southeast of Abisko in northern Sweden (68 22' N, 19 03'

191   E) (24) which is underlain by quartz-feldspar-rich sedimentary rock (Geological Survey of

192   Sweden). The study site is within the discontinuous permafrost region of northern Scandinavia

193   and consists of three distinct sub-habitats which are common to northern wetlands: (1) a well-

194   drained palsa underlain by permafrost, dominated by ericaceous and woody plants, (2) a bog

195   with variable water table depth and some active thawing, dominated by *Sphagnum* spp.

196   mosses, and (3) a fully-thawed and inundated fen, dominated by sedges such as *Eriophorum*

197   *angustifolium (19, 20).* In this study, the three sub-habitats were ordered following a temporal

198   succession of apparent time from "palsa", to "bog" and "fen" as has been done before (20)

199   following the classification of Johansson *et al* (2006) (19). The palsa and bog areas are

200   underlain by permafrost with a thickness of 10-20 m (25). The active layer, depending on the

201   surface topography, ranges from 0.5-1 m thickness at maximum thaw (25, 26). These three

202   thaw stages cover ~98% of the mire's non-lake surface (20). A thaw-dependent shift in these

203   habitats was observed from 1970 to 2000 during which palsa regions collapsed and bog and

204   fen areas increased by 17% (27). At the same time, an increase in average annual temperature

205   by 2.5°C between 1913 and 2006 was measured, resulting in an annual mean temperature

206   >0°C during the recent decades (28). The total precipitation also increased during this period

207   of time to an annual average of 306 mm (NORDKLIM, data available at

208   http://www.smhi.se/hfa_coord/nordklim). The expansion of wetlands after permafrost melt is a

209   widespread characteristic of peatlands affected by permafrost thawing (29-32) and the

210   successional shift from palsa to bog and fen areas has been documented in other northern

211   peatlands (31-34).

212   In July 2018, cores were taken in duplicates along a gently collapsing thaw gradient from palsa

213   to bog and fen (Fig. S1). Stordalen mire is a protected area with other ongoing field research,

214   thus the extent of coring is strictly limited due to the risk of accelerating permafrost thaw and/or

215   disturbance to other long-term measurements, especially at sensitive sites like erosion fronts.

216   However, extensive context data (https://polar.se/en/research-in-abisko/research-data/) from

217   the Abisko scientific community is available which ensures representative field sampling of a

218   heterogeneous permafrost area, with cores taken following a transect along the direction of

219   hydrological flow from palsa to bog and fen as described by Olefeldt and Roulet (2012) (35).

220   Given the restrictions in place, it was only possible to collect one core per location with two

221   locations sampled for each thaw stage (see also Fig. S1). A Humax corer of 50 cm length and

222   3-cm-diameter with inner core liners was used. The inner liners were washed three times with

223   80% ethanol, six times with sterile MilliQ water and sealed with sterilized butyl rubber stoppers

224   until coring. Butyl rubber stoppers were boiled three times in deionized water and sterilized at

225   121°C for 20 min in an autoclave. Sharp edges were cut into the end of the coring device to

226   help cut the peat layer. A hammer was used to further sample the active layer. Hammering

227   caused compaction of the cores. Therefore, the recorded depths are not comparable to the

228   initial soil profiles and the data is presented by different layers rather than depth. In the palsa

229   and bog area, cores were taken until the depth of the ground ice. Layers at the bottom of the

230   core which contained predominantly ice were excluded from further analyses. Therefore, the

231   soil investigated in this study represented the seasonally thawed active layer at Stordalen mire,

232   ranging from 30 to 49 cm. The cores were stored vertically at 4°C in the dark. Three cores

233   representing desiccating palsa, bog and fen were processed within 3-4 days (see also Fig.

234   S1). Due to detailed analysis of the first core set (Palsa A, Bog C and Fen E), additional cores

235   (Palsa B, Bog D and Fen F) from each thaw stage were analyzed after storage for 7 months

236   at 4°C in the dark, which is not ideal, but still could be used to determine if preservation of the

10

237   carbon by reactive iron was stable over longer time periods (Fig. S1). The long-term stored

238   core Palsa B still showed higher abundance of reactive iron minerals than Bog D and Fen F,

239   but less than Palsa A which could be due to natural variability, long-term storage or because

240   it was taken closer to the collapsing edge (Fig. S2). The cores A to F were compared to

241   triplicate cores previously collected in September 2017 at each thaw stage with a Pürckhauer

242   corer and processed directly after sampling, to show that the trends are representative for the

243   whole mire (Fig. S1). The replicate cores showed the same trends of 6 M HCl extractable iron.

244   Readily extractable Fe (defined by 0.5 M HCl extractable iron) showed similar trends to the

245   sodium dithionite citrate or hydroxylamine HCl extraction for all three thaw stages (Fig. S3).

246   The same trend of total organic carbon along the thaw gradient was observed (Fig S4).

247   **Porewater sampling and analysis**

248   The cores were kept in a vertical position during transfer into an anoxic glovebox (100% N_2).

249   Three different sections were identified by texture and color changes: (1) an organic horizon

250   on top, (2) a middle transition zone between the organic-rich and mineral-rich layer and (3) a

251   mineral horizon at the bottom (Fig. S1). Rhizon porewater samplers (Rhizosphere research

252   products, Netherlands) with a porous sampling area of 10 cm and 0.15 μm pore size were

253   used to extract porewater from three different depths, resulting in one sample representing

254   each organic horizon, transition zone and mineral horizon. The extracted porewater was

255   analyzed for dissolved Fe (total and Fe(II)), organic carbon (DOC) and fatty acids. The samples

256   were centrifuged for 5 min at 5300 g. For total Fe and Fe(II), the supernatant was acidified in

257   1 M hydrochloric acid (HCl) and quantified spectrophotometrically in triplicate with the ferrozine

258   assay (36). Dissolved OC was quantified in triplicate with a total organic carbon analyzer (High

259   TOC II, Elementar, Elementar Analysensysteme GmbH, Germany). High performance liquid

260   chromatography (HPLC; class VP with refractive index detector [RID] 10A and photo-diode

261   array detector SPD-M10A VP detectors; Shimadzu, Japan) was used to determine the fatty

262   acid concentrations.

Core splitting

The soil cores were removed from their liners under a N_2 atmosphere. Each core was sectioned into an organic horizon of varying thickness (4-10 cm), a transition zone (3-5 cm) and mineral horizon (4-10 cm) (Fig. S1). The transition zone represents the boundary between organic and mineral horizon and was additionally defined due to distinct geochemical conditions in the porewater analysis in the middle of the active layer near the boundary between organic and mineral horizon. Calculated bulk densities as a function of soil organic matter following Bockheim *et al* (2003) (37) were consistent with other studies conducted at Stordalen mire (38) (Palsa A: organic horizon: 0.03 ± 0.01 g/cm^3, transition zone: 0.08 ± 0.02 g/cm^3, mineral horizon: 0.84 ± 0.26 g/cm^3; Bog C: organic horizon 0.08 ± 0.01 g/cm^3, transition zone 1.29 ± 0.04 g/cm^3 and mineral horizon 1.74 ± 0.01 g/cm^3, Fen E: organic horizon 0.21 ± 0.02 g/cm^3, transition zone 1.97 ± 0.2 g/cm^3 and mineral horizon 1.72 ± 0.01 g/cm^3). Sub-samples were homogenized and weighed into 10 mL glass vials and kept frozen at -20°C prior to subsequent analysis.

Selective extractions

The soil layers were subjected to several chemical extractions to quantify the different iron phases. The soils were kept frozen prior to analysis, then dried at 20°C under anoxic conditions until no further weight loss was observed (less than 24 hours). 0.3 g dry soil was weighed into a 10 mL glass vial with 6.25 mL extractant and N_2 headspace. Prior to use, all glassware was washed with 1 M HCl for 10 min, flushed three times with deionized water and once with MilliQ water. Afterwards glassware was sterilized at 180°C in the oven for 4.5 hours. All samples were centrifuged at room temperature for 10 min at 5300 g. After centrifugation the supernatant was decanted into another 10 mL glass vial. Each extraction was performed in duplicates for each layer. Throughout the extraction, samples were kept in the dark under anoxic conditions (N_2 atmosphere). The extracts were analyzed for Fe and DOC as described above. Additionally, the samples were acidified in 1% (v/v) HNO_3 and analyzed in duplicates by MP-

289 AES/ICP-MS to get the total Fe, S, P and Al concentrations (Fig. S5). The illustrated iron values

290 throughout the whole study represent the iron values obtained by the ferrozine assay (for

291 differences in iron concentrations through the different analysis see Fig. S6). Due to dark color

292 of the extracts which can disturb the spectrophotometric measurement during ferrozine

293 complexation, the absorbance of blanks (sample diluted in 1 M HCl or hydroxylamine-HCl) was

294 measured before ferrozine addition and later subtracted to avoid overestimation of iron

295 concentrations. The trends of all Fe analysis (ferrozine assay, MP-AES/ICP-MS analysis) show

296 all the same iron trends with depth and along the thaw gradient (Fig. S6). For additional

297 extractant-specific experimental parameters see below.

298 *6 M HCl*

299 To quantify the total extractable Fe of the soil layers, dried samples were subjected to a 70°C

300 6 M HCl extraction for 24 h (39, 40).

301 *Sodium pyrophosphate*

302 The sodium pyrophosphate extraction was performed following Coward *et al* (2017) (10) at pH

303 10 to determine the colloidal or OM-chelated iron.

304 *Hydroxylamine-HCl*

305 To extract the short ranged ordered (SRO) Fe oxides, an acidic hydroxylamine-HCl (pH <2)

306 extraction was carried out under the same conditions as the sodium pyrophosphate extraction

307 (10).

308 *Dithionite-citrate*

309 Extractions were conducted using a solution of 0.27 M trisodium citrate, 0.11 M sodium

310 bicarbonate and 0.1 M sodium dithionite (total ionic strength: 1.85 M), as previously described

311 (12). This extraction was used to also quantify the reactive iron minerals but in particular the

312 organic molecules binding to it (released during iron mineral dissolution). Instead of heating to

13

313   80°C as described by Lalonde *et al* (2012) (12), the dithionite-citrate extraction was performed

314   under the same conditions as the sodium pyrophosphate and hydroxylamine-HCl extraction

315   (on a rolling shaker at room temperature for 16h) for better comparison between the different

316   extractions. The citrate addition as a metal ion complexing agent was necessary to avoid

317   under-estimation of iron and organic carbon as a result of complexation or mineral precipitation

318   during extraction. Without citrate addition, we obtained 64±3% less iron and 57±28% less

319   carbon after sodium dithionite reductive dissolution. As described in Lalonde *et al* (2012) (12),

320   we also used a 1.85 M sodium chloride/0.11 M sodium bicarbonate extraction as a control

321   experiment under the same conditions (same solid:solution ratio, temperature, time, ionic

322   strength) to distinguish between organic carbon (OC) which is readily desorbed and organic

323   carbon which is released by the reduction of iron(III) minerals. To determine the DOC

324   background concentrations caused by the trisodium citrate, blanks (trisodium citrate sodium

325   bicarbonate solution) were analyzed during each measurement. The background

326   concentration was later subtracted from the total DOC value, as well as the DOC concentration

327   of the control experiment (sodium chloride sodium bicarbonate solution), resulting in the OC

328   which is released by the reduction of reactive iron (see also Fig. S7).

329   **TOC analysis**

330   To quantify the total organic carbon (TOC), soil samples from each layer were dried at 60°C

331   until the weight remained constant. The dry soils were then ground and acidified with 16% HCl

332   to remove the inorganic carbon. After washing with deionized water and subsequent drying,

333   the TOC content was analyzed by an Elementar vario El (Elementar Analysensysteme GmbH,

334   Germany). The TOC content goes in line with previously reported values (41).

335   **EXAFS/XANES analysis**

336   Samples were dried under an N_2 atmosphere and stored anoxically in a glove box prior to

337   analysis. Sample were then sealed in plastic multi-sample holders with Kapton polyimide tape

338   and kept anoxic until they were transferred to a sample mount at the beamline. The sample

339 holder was in a cryostat during analysis to limit beam damage and to prevent oxidation of

340 Fe(II). Reference samples such as natural nontronite and ferrosmectite (referred to as Fe

341 clays) were obtained from the Clay Mineral Society. Fe(II)-citrate and Fe(III)-citrate were used

342 as reference samples for Fe(II)-OM and Fe(III)-OM, and were prepared and analysed as

343 described in Daugherty *et al* (2017) (42). Mackinawite, used as a reference for FeS, was

344 prepared and analysed as described in Troyer *et al* (2014) (43). 2-line ferrihydrite, prepared

345 and analysed as described in Borch *et al* (2007) (44), was used as a reference for poorly

346 crystalline Fe.

347 Fe K-edge X-ray absorption spectroscopic analyses were conducted at Beamline 11−2 at the

348 Stanford Synchrotron Radiation Light source (SSRL) in Menlo Park, CA. The Si(220) phi = 0°

349 monochromator was used, and beam size of 1 mm vertical and 10 mm horizontal. Iron X-ray

350 absorption near edge structure (XANES) and EXAFS fluorescence spectra were collected with

351 the PIPS detector simultaneously with the transmission spectrum of Fe foil, which was used

352 for internal energy calibrations. Multiple scans (3-4) per sample were acquired as necessary

353 to achieve satisfactory data quality.

354 Scans were calibrated to 7112 eV (the first inflection point of Fe(0), and then averaged over 3

355 or 4 scans using SixPack software. They were deglitched at 7250 and 7600 eV, and then

356 normalized with the E0 value, determined by finding the inflection point of the first derivative of

357 each sample. Linear combination fitting (LCF) of EXAFS spectra was performed in SixPack

358 from chi values of 2 to 12 with an x-weight of 3. Non-negative fits were performed, and

359 components were chosen based on prior knowledge of the sample mineralogy.

360 **Correlative SEM and nanoSIMS**

361 The two end-members, palsa and fen, were analyzed using SEM and nanoSIMS (see also

362 Figs. S8 and S9) using only the free particles of the fine fraction of the transition zone and the

363 mineral horizon. As described by Kopittke *et al* (2018) (45) and Keiluweit *et al* (2012) (46),

364 subsamples of each layer (1 mg) were dispersed in 10 mL of anoxic deionized water and gently

365   shaken to obtain the free organo-mineral particles from the fine fraction of the soil. 100 µl of

366   the suspension was placed onto a silica wafer and dried under an N_2 atmosphere. The samples

367   were sputter-coated with 12 nm platinum (Pt) using a Bal-Tec SCD005 sputter coater.

368   To characterize the organo-mineral particles of the fine fraction by size and crystallinity and

369   identify representative particles, a field emission scanning electron microscope (FE-SEM; Jeol

370   JSM-6500F), equipped with secondary electron detector, was used prior to nanoSIMS

371   analysis. The acceleration voltage was set to 5 kV, with a working distance of 10 mm.

372   The nanoSIMS analysis were performed at the Cameca nanoSIMS 50L of the Chair of Soil

373   Science (TU München, Germany). Prior to the measurements, the samples were additionally

374   coated with Au/Pd layer (~30 nm) to avoid charging during the analysis. The Cs^+ primary ion

375   beam was used with a primary ion impact energy of 16 keV. Prior to the final measurement,

376   any potential contaminants and the Au/Pd coating layer were sputtered away at 50 x 50 µm

377   with a high primary beam current (pre-sputtering). To enhance the secondary ion yields, Cs^+

378   ions were implanted into the sample during this pre-sputtering process. The primary beam

379   (~1.2 pA) was focused at a lateral resolution ~100 nm and scanned over the sample with $^{12}C^-$

380   , $^{16}O^-$, $^{12}C^{14}N^-$, $^{31}P^-$, $^{32}S^-$, $^{27}Al^{16}O^-$ and $^{56}Fe^{16}O^-$ secondary ions collected using electron

381   multipliers. To compensate for any charging of the non-conductive mineral particles, the

382   electron flood gun was used. All analyses were performed in imaging mode. For every layer,

383   four representative spots were analyzed to obtain a reliable data basis for the spatial

384   distribution of $^{12}C^-$ and $^{56}Fe^{16}O^-$. Ion images of 30 x 30 µm field of view, 30 planes with a dwell

385   time of 1 ms/pixel, 256 pixels x 256 pixels were recorded. The estimated depth resolution with

386   16 keV Cs^+ ions was 10 nm.

387   Finally, the nanoSIMS images were analyzed using the Open MIMS Image plugin available

388   within ImageJ (available free-of-charge at, https:// imagej.nih.gov/ij/). All presented images

389   were corrected for the electron multiplier dead time (44 ns), as well as drift corrected, and the

390   planes accumulated. A median filter was applied on all images.

Most-probable-number (MPN) counts

Most-probable number (MPN) counts were performed on the soil samples from the different depths of the cores in seven replicates. MPNs were set up in 96-well plates with liquid media for quantification of Fe(III)-reducing bacteria (47, 48). 5 mM sodium acetate, 5 mM sodium lactate and 5 mM 2-line ferrihydrite (chemically synthesized as previously described (48)) were added to the anoxic media (0.6 g/L KH_2PO_4, 0.3 g/L NH_4Cl, 0.025 g/LMgSO$_4$ x 7 H$_2$0, 0.4 g/L MgCl$_2$ x 6 H$_2$0, CaCl$_2$ x 2 H$_2$0, 22 mM NaHCO$_3$, 1 mL/L trace element according to Widdel et al (1983) (49), 1 mL/L vitamin solution after Widdel & Pfennig (1981) (50) and 1 mL/L selenite/tungstate solution according to Widdel (1980) (51)). To calculate the cell numbers (cells/g soil) from the positive MPN wells, the software program KLEE was used applying confidence limits of Cornish and Fisher (1938) (52) and the bias correction after Salam (1978) (53, 54).

Acknowledgments

References

1. C. C. Mu *et al.*, Soil organic carbon stabilization by iron in permafrost regions of the Qinghai-Tibet Plateau. *Geophys Res Lett* **43**, 10286-10294 (2016).

2. T. I. Eglinton, Geochemistry: A rusty carbon sink. *Nature* **483**, 165-166 (2012).

417   3..   C. Tarnocai *et al.*, Soil organic carbon pools in the northern circumpolar permafrost region.

418   *Global Biogeochem Cy* **23**, GB2023 (2009).

419   4.   S. A. Zimov, E. A. G. Schuur, F. S. Chapin, Permafrost and the global carbon budget. *Science*

420   **312**, 1612-1613 (2006).

421   5.   E. A. G. Schuur *et al.*, Climate change and the permafrost carbon feedback. *Nature* **520**, 171-

422   179 (2015).

423   6.   L. D. Hinzman *et al.*, Trajectory of the Arctic as an integrated system. *Ecol Appl* **23**, 1837-1868

424   (2013).

425   7.   R. K. Pachauri *et al.* (2014):   Climate Change 2014: Synthesis Report. Contribution of

426   Working Groups I, II and III to the Fifth Assessment Report of the Intergovernmental Panel on

427   Climate Change, Geneva, Switzerland, IPCC, 151 p., ISBN: 978-92-9169-143-2.

428   8.   C. Estop-Aragones *et al.*, Limited release of previously-frozen C and increased new peat

429   formation after thaw in permafrost peatlands. *Soil Biol Biochem* **118**, 115-129 (2018).

430   9.   M. Shimizu *et al.*, Dissimilatory Reduction and Transformation of Ferrihydrite-Humic Acid

431   Coprecipitates. *Environ Sci Technol* **47**, 13375-13384 (2013).

432   10.   E. K. Coward, A. T. Thompson, A. F. Plante, Iron-mediated mineralogical control of organic

433   matter accumulation in tropical soils. *Geoderma* **306**, 206-216 (2017).

434   11.   M. Kleber, R. Mikutta, M. S. Torn, R. Jahn, Poorly crystalline mineral phases protect organic

435   matter in acid subsoil horizons. *Eur J Soil Sci* **56**, 717-725 (2005).

436   12.   K. Lalonde, A. Mucci, A. Ouellet, Y. Gelinas, Preservation of organic matter in sediments

437   promoted by iron. *Nature* **483**, 198-200 (2012).

438   13.   T. Riedel, D. Zak, H. Biester, T. Dittmar, Iron traps terrestrially derived dissolved organic matter

439   at redox interfaces. *P Natl Acad Sci USA* **110**, 10101-10105 (2013).

440   14.   E. M. Herndon *et al.*, Pathways of anaerobic organic matter decomposition in tundra soils from

441   Barrow, Alaska. *J Geophys Res-Biogeo* **120**, 2345-2359 (2015).

442   15.   D. A. Lipson, M. Jha, T. K. Raab, W. C. Oechel, Reduction of iron (III) and humic substances

443   plays a major role in anaerobic respiration in an Arctic peat soil. *J Geophys Res-Biogeo* **115**,

444   G00I06 (2010).

445   16.   D. Olefeldt, M. R. Turetsky, P. M. Crill, A. D. McGuire, Environmental and physical controls on

446   northern terrestrial methane emissions across permafrost zones. *Global Change Biol* **19**, 589-

447   603 (2013).

448   17.   M. R. Turetsky *et al.*, Short-term response of methane fluxes and methanogen activity to water

449   table and soil warming manipulations in an Alaskan peatland. *J Geophys Res-Biogeo* **113**,

450   G000496 (2008).

451   18.   D. Zona *et al.*, Methane fluxes during the initiation of a large-scale water table manipulation

452   experiment in the Alaskan Arctic tundra. *Global Biogeochem Cy* **23**, GB2013 (2009).

453   19.   T. Johansson *et al.*, Decadal vegetation changes in a northern peatland, greenhouse gas fluxes

454   and net radiative forcing. *Global Change Biol* **12**, 2352-2369 (2006).

455   20.   S. B. Hodgkins *et al.*, Changes in peat chemistry associated with permafrost thaw increase

456   greenhouse gas production. *P Natl Acad Sci USA* **111**, 5819-5824 (2014).

457   21.   C. K. McCalley *et al.*, Methane dynamics regulated by microbial community response to

458   permafrost thaw. *Nature* **514**, 478-481 (2014).

459   22.   O. P. Mehra, M. L. Jackson, Iron oxide removal from soils and clays by a dithionite-citrate

460   system buffered with sodium bicarbonate. *Clays Clay Min.* **7**, 317-327 (1958).

461   23.   R. Wagai, L. M. Mayer, Sorptive stabilization of organic matter in soils by hydrous iron oxides.

462   *Geochim Cosmochim Ac* **71**, 25-35 (2007).

463   24.   R. Mondav *et al.*, Discovery of a novel methanogen prevalent in thawing permafrost. *Nat*

464   *Commun* **5**, 3212 (2014).

465   25.   H. J. Akerman, M. Johansson, Thawing permafrost and thicker active layers in sub-arctic

466   Sweden. *Permafrost Periglac* **19**, 279-292 (2008).

467   26.   J. Klaminder, K. Yoo, J. Rydberg, R. Giesler, An explorative study of mercury export from a

468   thawing palsa mire. *J Geophys Res-Biogeo* **113**, G000776 (2008).

469   27.   N. Malmer, T. Johansson, M. Olsrud, T. R. Christensen, Vegetation, climatic changes and net

470   carbon sequestration in a North-Scandinavian subarctic mire over 30 years. *Global Change Biol*

471   **11**, 1895-1909 (2005).

472   28.   T. V. Callaghan *et al.*, A new climate era in the sub-Arctic: Accelerating climate changes and

473   multiple impacts. *Geophys Res Lett* **37**, L14705 (2010).

474   29.   M. T. Jorgenson, C. H. Racine, J. C. Walters, T. E. Osterkamp, Permafrost degradation and
475   ecological changes associated with a warming climate in central Alaska. *Climatic Change* **48**,
476   551-579 (2001).

477   30.   J. A. O'Donnell *et al.*, The Effects of Permafrost Thaw on Soil Hydrologic, Thermal, and Carbon
478   Dynamics in an Alaskan Peatland. *Ecosystems* **15**, 213-229 (2012).

479   31.   S. Payette, A. Delwaide, M. Caccianiga, M. Beauchemin, Accelerated thawing of subarctic
480   peatland permafrost over the last 50 years. *Geophys Res Lett* **31**, GL020358 (2004).

481   32.   D. H. Vitt, L. A. Halsey, S. C. Zoltai, The changing landscape of Canada's western boreal forest:
482   the current dynamics of permafrost. *Can J Forest Res* **30**, 283-287 (2000).

483   33.   W. L. Quinton, M. Hayashi, L. E. Chasmer, Permafrost-thaw-induced land-cover change in the
484   Canadian subarctic: implications for water resources. *Hydrol Process* **25**, 152-158 (2011).

485   34.   S. C. Zoltai, Cyclic Development of Permafrost in the Peatlands of Northwestern Alberta,
486   Canada. *Arctic Alpine Res* **25**, 240-246 (1993).

487   35.   D. Olefeldt, N. T. Roulet, Effects of permafrost and hydrology on the composition and transport
488   of dissolved organic carbon in a subarctic peatland complex. *J Geophys Res-Biogeo* **117**,
489   G01005 (2012).

490   36.   L. L. Stookey, Ferrozine - a New Spectrophotometric Reagent for Iron. *Anal Chem* **42**, 779-781
491   (1970).

492   37.   J. G. Bockheim, K. M. Hinkel, F. E. Nelson, Predicting carbon storage in tundra soils of arctic
493   Alaska. *Soil Sci Soc Am J* **67**, 948-950 (2003).

494   38.   B. E. Rydén, L. Fors, L. Kostov, Physical properties of the tundra soil-water system at Stordalen,
495   Abisko. *Ecological Bulletins* **30**, 27-54 (1980).

496   39.   R. C. Aller, J. E. Mackin, R. T. Cox, Diagenesis of Fe and S in Amazon Inner Shelf Muds -
497   Apparent Dominance of Fe Reduction and Implications for the Genesis of Ironstones. *Cont Shelf*
498   *Res* **6**, 263-289 (1986).

499   40.   S. W. Poulton, D. E. Canfield, Development of a sequential extraction procedure for iron:
500   implications for iron partitioning in continentally derived particulates. *Chem Geol* **214**, 209-221
501   (2005).

502   41.   M. Lupascu, J. L. Wadham, E. R. C. Hornibrook, R. D. Pancost, Temperature Sensitivity of
503   Methane Production in the Permafrost Active Layer at Stordalen, Sweden: a Comparison with
504   Non-permafrost Northern Wetlands. *Arct Antarct Alp Res* **44**, 469-482 (2012).

505   42.   E. E. Daugherty, B. Gilbert, P. S. Nico, T. Borch, Complexation and Redox Buffering of Iron(II)
506   by Dissolved Organic Matter. *Environ Sci Technol* **51**, 11096-11104 (2017).

507   43.   L. D. Troyer, Y. Tang, T. Borch, Simultaneous reduction of arsenic(V) and uranium(VI) by
508   mackinawite: role of uranyl arsenate precipitate formation. *Environ Sci Technol* **48**, 14326-
509   14334 (2014).

510   44.   T. Borch, Y. Masue, R. K. Kukkadapu, S. Fendorf, Phosphate imposed limitations on biological
511   reduction and alteration of ferrihydrite. *Environ Sci Technol* **41**, 166-172 (2007).

512   45.   P. M. Kopittke *et al.*, Nitrogen-rich microbial products provide new organo-mineral associations
513   for the stabilization of soil organic matter. *Global Change Biol* **24**, 1762-1770 (2018).

514   46.   M. Keiluweit *et al.*, Nano-scale investigation of the association of microbial nitrogen residues
515   with iron (hydr)oxides in a forest soil O-horizon. *Geochim Cosmochim Ac* **95**, 213-226 (2012).

516   47.   E. D. Melton, A. Rudolph, S. Behrens, C. Schmidt, A. Kappler, Influence of Nutrient
517   Concentrations on MPN Quantification and Enrichment of Nitrate-Reducing Fe(II)-Oxidizing and
518   Fe(III)-Reducing Bacteria from Littoral Freshwater Lake Sediments. *Geomicrobiol J* **31**, 788-
519   801 (2014).

520   48.   K. L. Straub, A. Kappler, B. Schink, Enrichment and isolation of ferric-iron- and humic-acid-
521   reducing bacteria. *Method Enzymol* **397**, 58-77 (2005).

522   49.   F. Widdel, G. W. Kohring, F. Mayer, Studies on Dissimilatory Sulfate-Reducing Bacteria That
523   Decompose Fatty-Acids .3. Characterization of the Filamentous Gliding Desulfonema-Limicola
524   Gen-Nov Sp-Nov, and Desulfonema-Magnum Sp-Nov. *Arch Microbiol* **134**, 286-294 (1983).

525   50.   F. Widdel, N. Pfennig, Studies on Dissimilatory Sulfate-Reducing Bacteria That Decompose
526   Fatty-Acids .1. Isolation of New Sulfate-Reducing Bacteria Enriched with Acetate from Saline
527   Environments - Description of Desulfobacter-Postgatei Gen-Nov, Sp-Nov. *Arch Microbiol* **129**,
528   395-400 (1981).

529   51.   F. Widdel, Anaerobic degradation of fatty acdis and benzoic acid by newly isolated species
530   sulphate-reducing bacteria. *Dissertation, University Goettingen, FRG* (1980).

21

531   52.   E. A. F. Cornish, R. A. Fisher, Moments and cumulants in the specification of distributions.

532   *Revue de l'Institut International de Statistique/Rev. Int. Stat. Inst. 5* **4**, 307-320 (1938).

533   53.   A. J. Klee, A Computer-Program for the Determination of Most Probable Number and Its

534   Confidence-Limits. *J Microbiol Meth* **18**, 91-98 (1993).

535   54.   I. A. K. Salama, G. G. Koch, H.D. Tolley, On the estimation of the most probable number in a

536   serial dilution technique. *Commun. Stat. - Theory Methods* **A7**, 1267-1281 (1978).

537

538

539 **Figures and Tables**
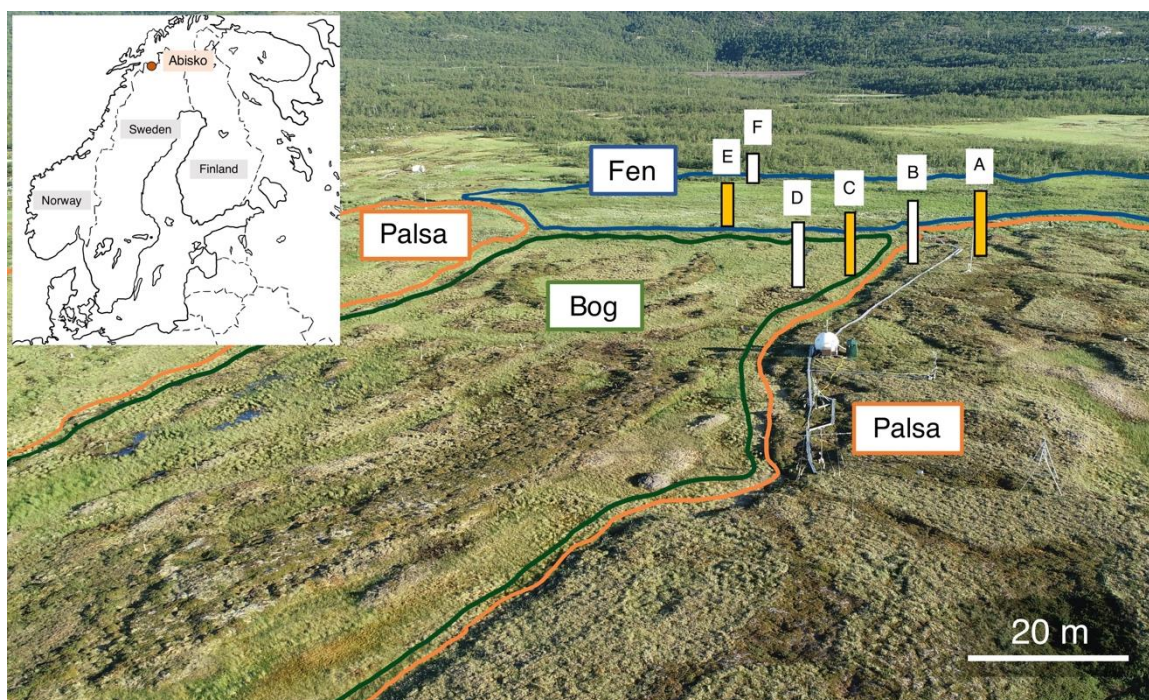
540

541 **Fig. 1.** Field site Stordalen mire close to Abisko in the North of Sweden. The three main thaw stages

542 are (1) palsa (marked in orange), (2) bog (in green) and (3) fen (in blue). The positions of the three cores

543 analyzed in detail within 3-4 days of collection, which represent all three thaw stages, are shown in

544 yellow. Additional cores (shown in white) were taken and analyzed after 7 months of incubation at 4°C

545 (Fig. S1).

546
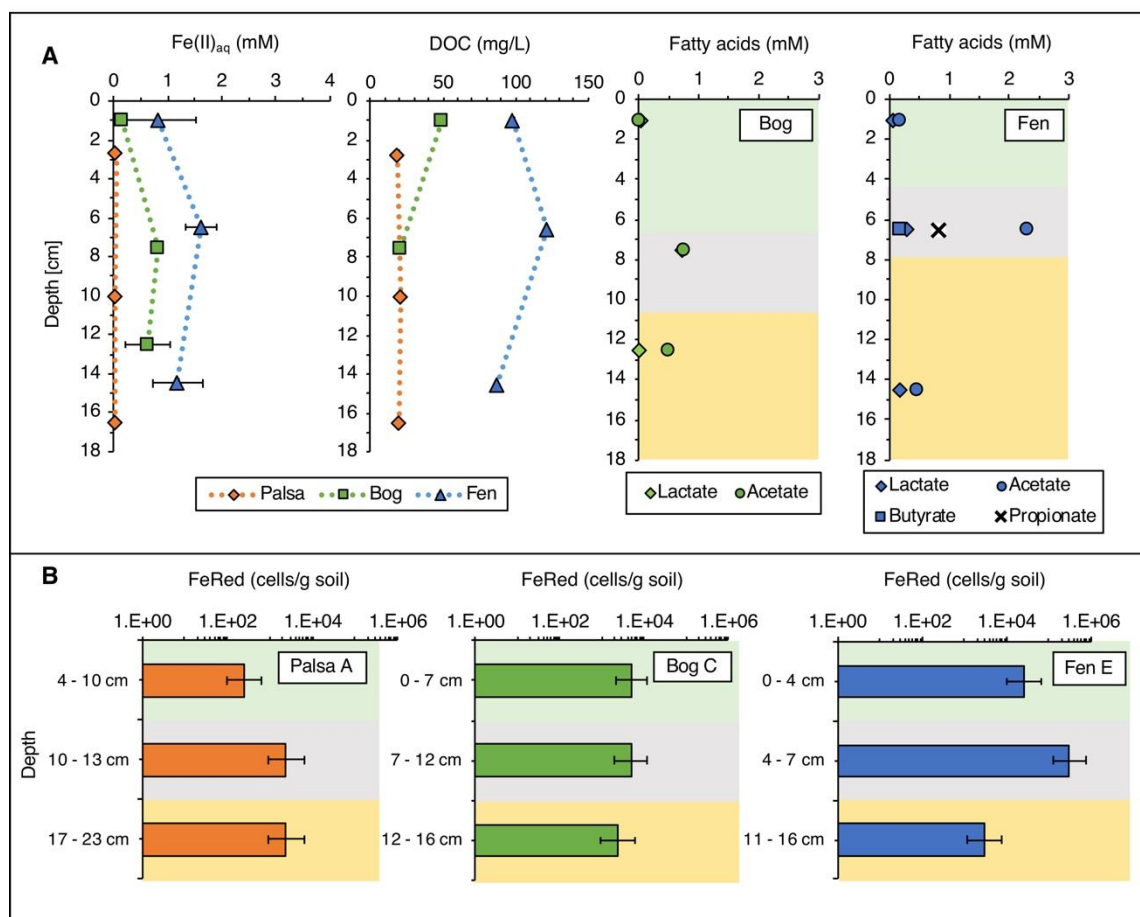
Fig. 2. *(A)* Porewater geochemical analysis of the cores Palsa A, Bog C and Fen E and *(B)*, most probable number quantifications of Fe(III)-reducing bacteria (FeRed) in the solid phase of the cores Palsa A, Bog C and Fen E along the thaw gradient. The error bars of the porewater data represent triplicate measurements. The error bars of the most probable number estimations of Fe(III)-reducers represent 7 replicate analyses and indicate lower and upper limits of the 95% confidence intervals. Please note the differences in the scale of y-axis due to variable thickness of each soil layer along the thaw gradient. The green background marks the organic horizon, grey the transition zone, and yellow the mineral horizon.
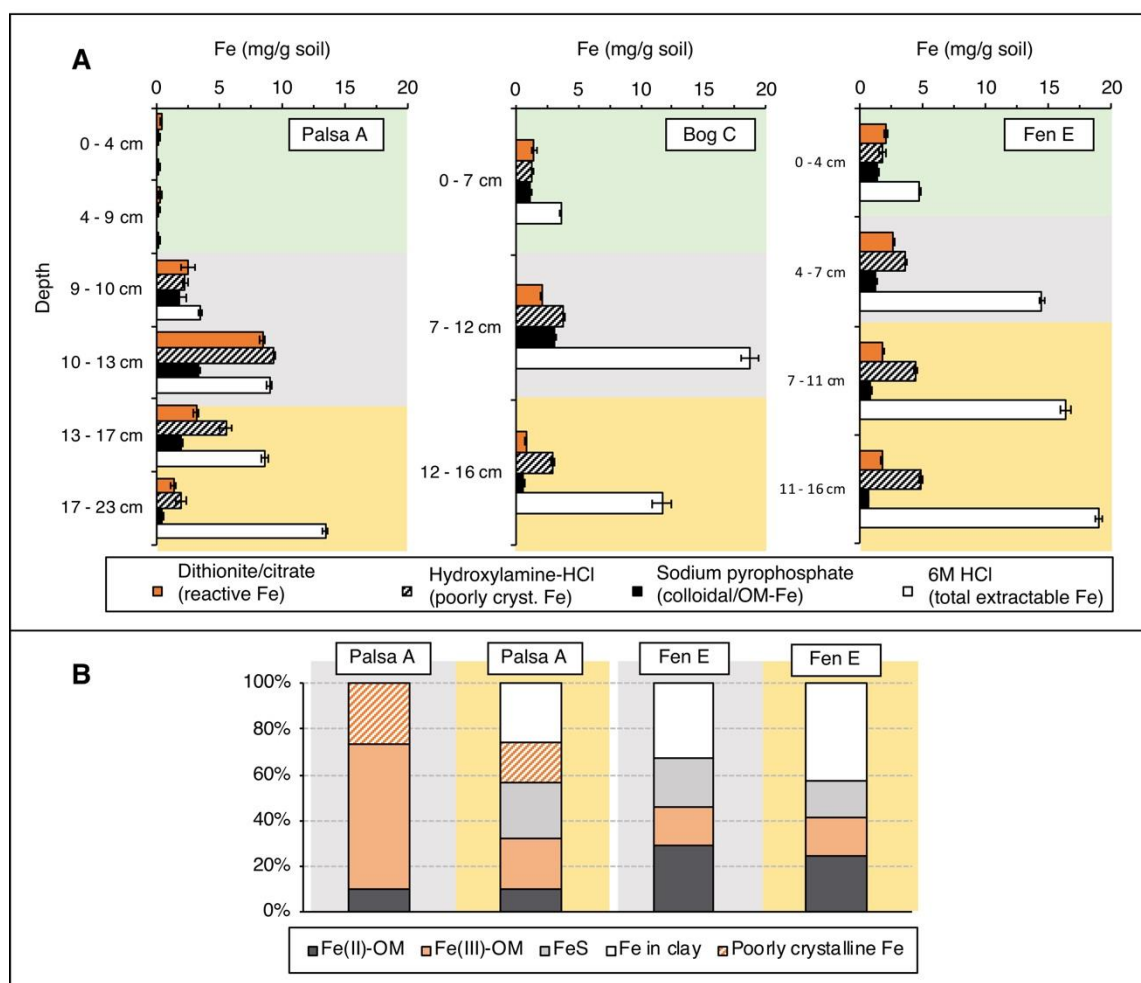
Fig. 3. Fe speciation along the thaw gradient determined by *(A)* selective extractions and *(B)* EXAFS. The reactive iron mineral fraction [mg Fe per g soil] was quantified in the different layers and compared to the total extractable Fe (6M HCl extractable Fe, referred to mg Fe(tot) per g soil in the text) and to the colloidal and/or OM-chelated Fe. Please note the differences in the scale of y-axis due to variable thickness of each soil layer along the thaw gradient. The green background marks the organic horizon, grey the transition zone, and yellow the mineral horizon. Error bars represent duplicate extractions of each layer per thaw stage. EXAFS results of the transition zone and the mineral horizon of the two-end members palsa and fen show loss of the poorly crystalline Fe (reference probe: 2-line ferrihydrite), the decrease in OM-chelated Fe (reference probes: Fe(II)-citrate and Fe(III)-citrate), the increase of Fe in clays (reference probes: natural nontronite and ferrosmectite) and Fe sulfur species (reference probe: mackinawite) with depth and along the thaw gradient.
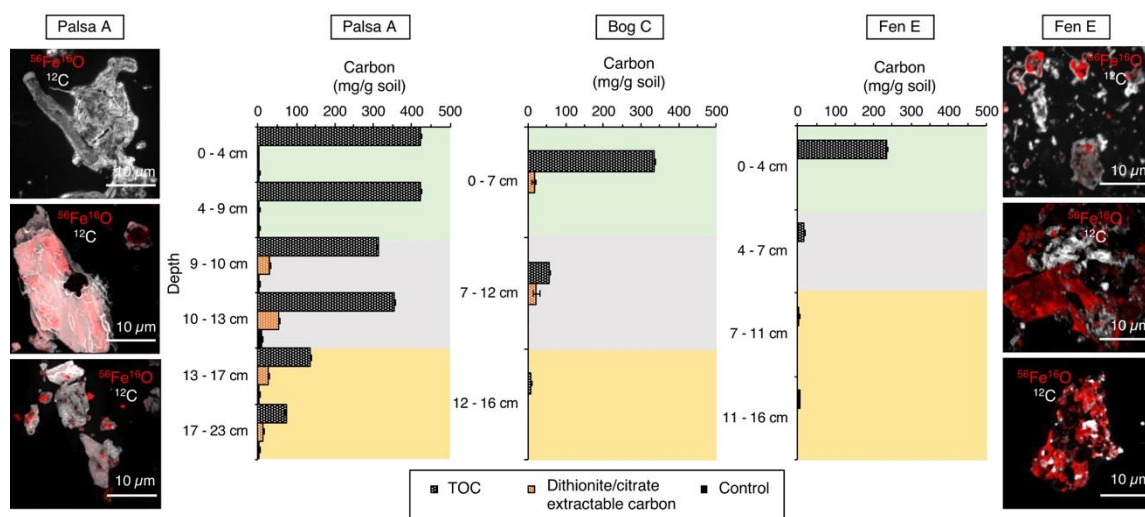
Fig. 4. Left and right: High spatial resolution analysis of iron-carbon associations by nanoSIMS along the thaw gradient (two end-members palsa (left) and fen (right)). The strong spatial association of C to Fe(III) minerals could only be observed in the palsa transition zone. The other fine fractions showed organic-free iron minerals. For the two end-members palsa and fen, four particles of the fine fractions of each layer were analyzed by nanoSIMS, all showing the same spatial distribution of Fe and C as shown by these six representatives (see also Figs. S8 and S9). Middle: Carbon bound by reactive iron minerals along the thaw gradient. The carbon which dislodged from the soil during the reductive dissolution of reactive iron oxides (orange) is shown in comparison to the total organic carbon determined via combustion (black grids, labeled as TOC). The control (same ionic strength and same pH as the sodium dithionite citrate extraction) shows negligible carbon release (Table S1). Errors indicate the range of duplicate analyses of each layer in each thaw stage.

Supplementary Information for

# Iron mineral dissolution during permafrost thaw releases associated organic carbon

Monique S. Patzner[1], Carsten W. Mueller[2], Miroslava Malusova[1], Verena Nikeleit[1], Thomas Scholten[3], Carmen Hoeschen[2], James M. Byrne[1], Thomas Borch[4], Andreas Kappler[1] & Casey Bryce[1]*

* Casey Bryce

**Email:** casey.bryce@uni-tuebingen.de

582
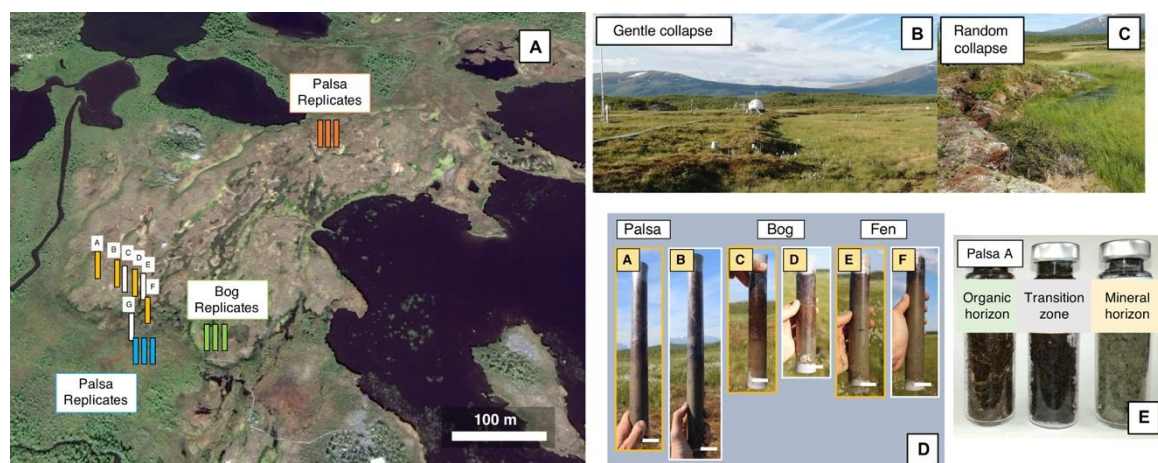
Fig. S1. *(A)* Position of cores taken along a thaw gradient at Stordalen mire (Abisko, Sweden). Cores A to F were taken with a Humax corer and sterile plastic liners in June 2018. Yellow: Cores were immediately split and processed after sampling (3-4 days). White: Cores were stored at 4 °C for 7 months and then processed. The data was compared to triplicate cores in each thaw stage (Palsa in orange, Bog in green and Fen in blue) which were taken with a Pürckhauer corer in September 2017 and immediately processed after sampling. All cores showed the same trend for total extractable iron, for the poorly crystalline iron and the total carbon along the thaw gradient. *(B)* Gentle collapse of palsa sites at Stordalen mire (Abisko, Sweden). The sampled thaw gradient represents a gentle collapse of palsa to bog and is not randomly collapsing. *(C)* Random collapse of palsa sites at Stordalen mire (Abisko, Sweden). Permafrost thaw does not necessarily progress through all three thaw stages (palsa, bog and fen). Rapid thaw can also create randomly collapsing palsa sites which subsequently become more like a fen. *(D)* Cores taken along a thaw gradient. Palsa: Core A (68°21'18.70"N, 19° 2'38.00"E) and core B (68°21'18.50"N, 19° 2'38.80"E) showed the three main layers in the palsa area: (1) organic horizon, (2) transition zone and (3) mineral horizon. The organic layer was dry and oxic. Bog: Core C (68°21'18.60"N, 19° 2'39.20"E) and core D (68°21'18.30"N, 19° 2'40.00"E) clearly showed the division into the three layers: (1) organic horizon, (2) transition zone and (3) mineral horizon. Both cores were completely water saturated. Fen: Core E (68°21'16.80"N, 19° 2'40.30"E) and core F (68°21'17.80"N, 19° 2'41.30"E) also showed the three layers and were water saturated. The cores represent the active layer in July 2018. Yellow: Core A, C and E were immediately split and processed (3-4 days). White: Core C, E and G were stored for 7 months. The Scale bar = 3 cm. *(E)* Example of the subdivision into (1) organic horizon, (2) transition zone and (3) mineral horizon (Palsa A). The cores were split under an N_2 atmosphere and immediately frozen in 10 mL glass vials at -20°C till further analysis.
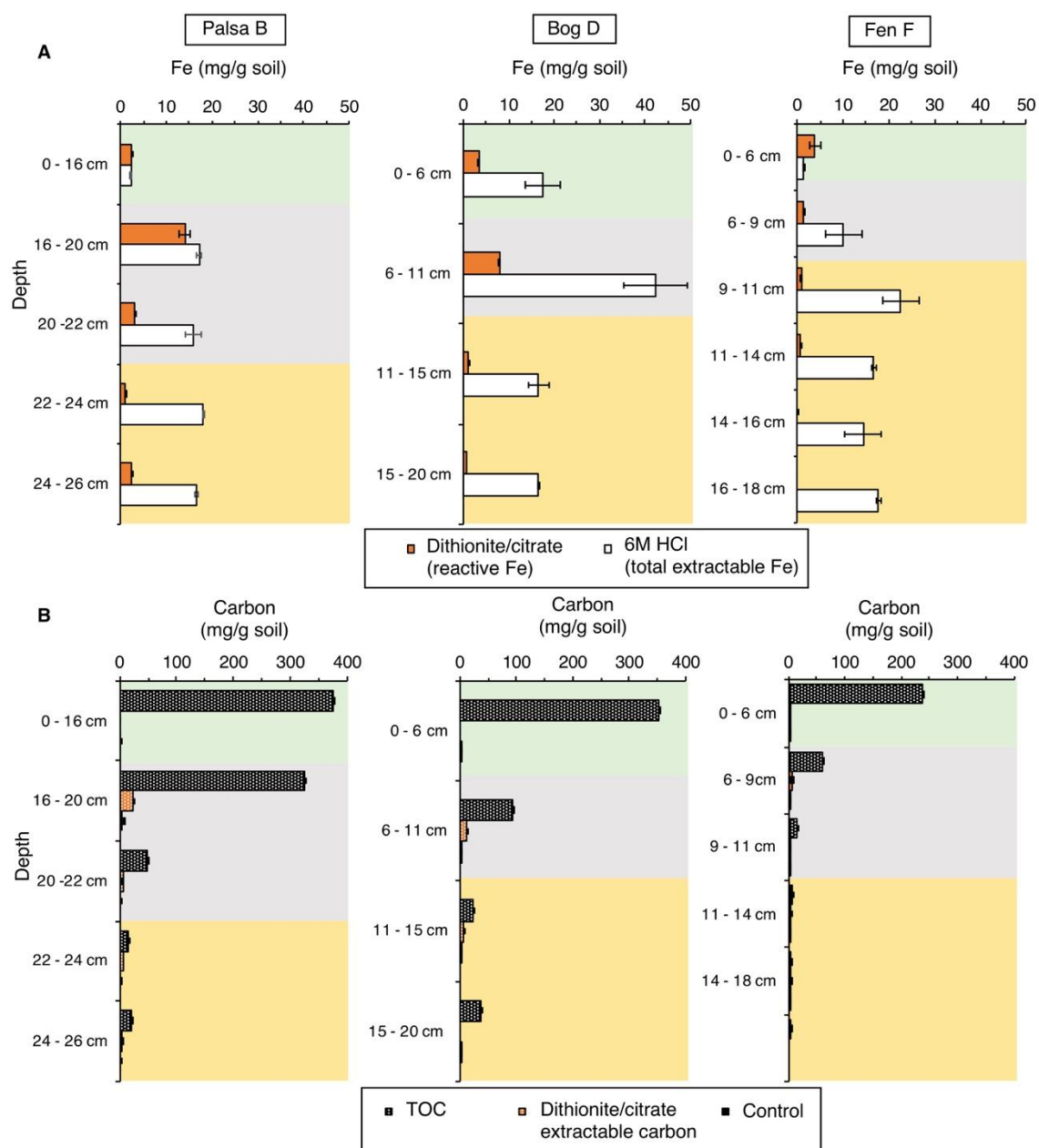
Fig. S2. Extractions of replicate cores. *(A)* Iron and *(B)* carbon concentration of cores Palsa B, Bog D and Fen F. Cores were split after 7 months of incubation at 4°C. The green box marks the organic horizon, grey box the transition zone and yellow box the mineral horizon. Errors indicate the range of duplicate analyses of each layer in each thaw stage. TOC was determined via combustion, whereas the carbon in the dithionite citrate and the control extract (sodium chloride bicarbonate) was determined with the carbon analyzer.

614
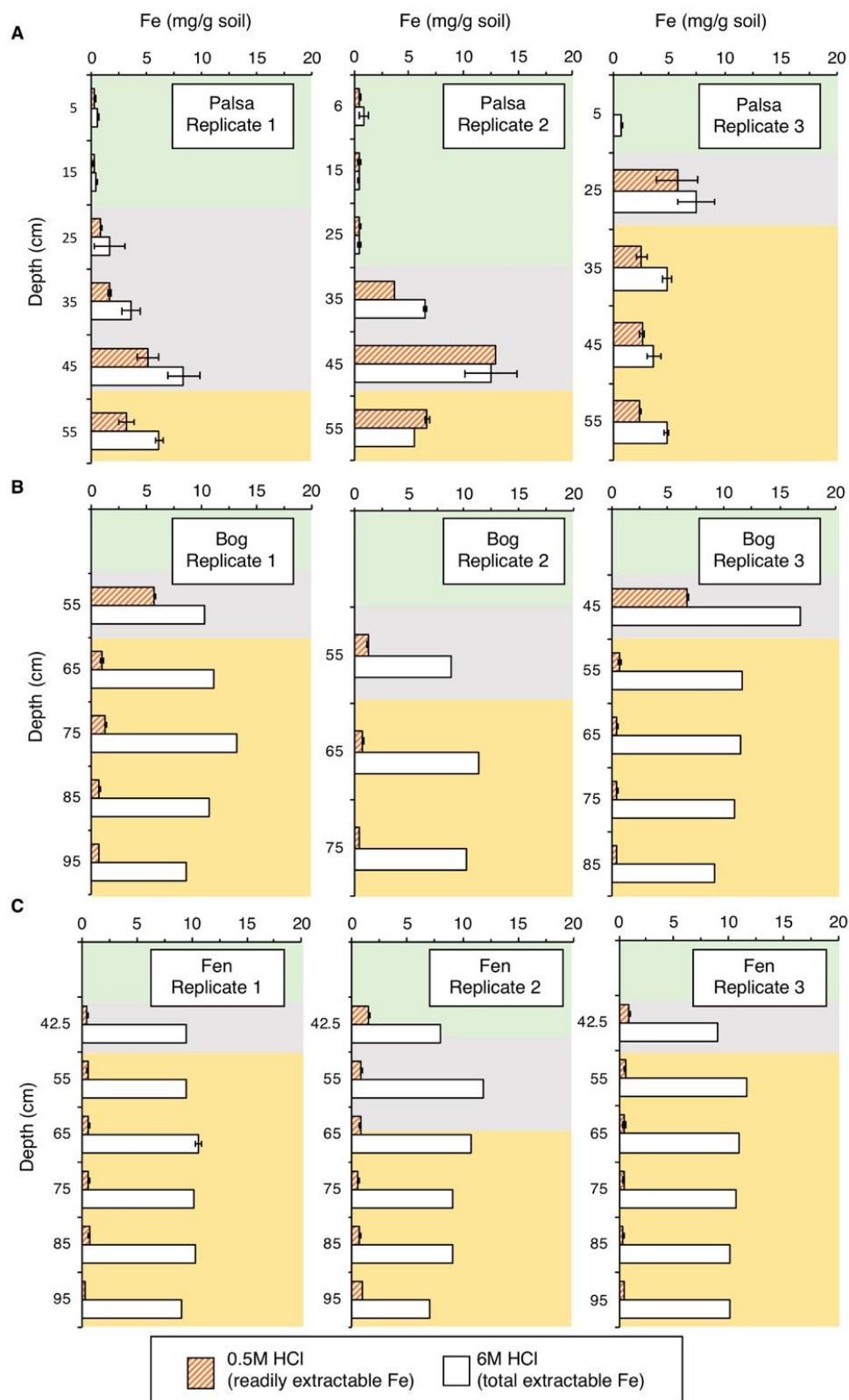
Fig. S3. Iron extractions of replicate cores taken with a Pürckhauer corer: *(A)* Palsa (68°21'26.56"N, 19° 3'0.19"E), *(B)* Bog (68°21'16.02"N, 19° 2'49.21"E), (C) Fen (68°21'17.16"N, 19° 2'36.29"E).

617   Each core was divided into layers in the field and immediately processed. All replicates represent

618   the active layer in September 2017. The bog and the fen soils were waterlogged. The green box

619   marks the organic horizon, grey box the transition zone and yellow box the mineral horizon. Errors

620   indicate the range of duplicate analyses of each layer in each thaw stage.
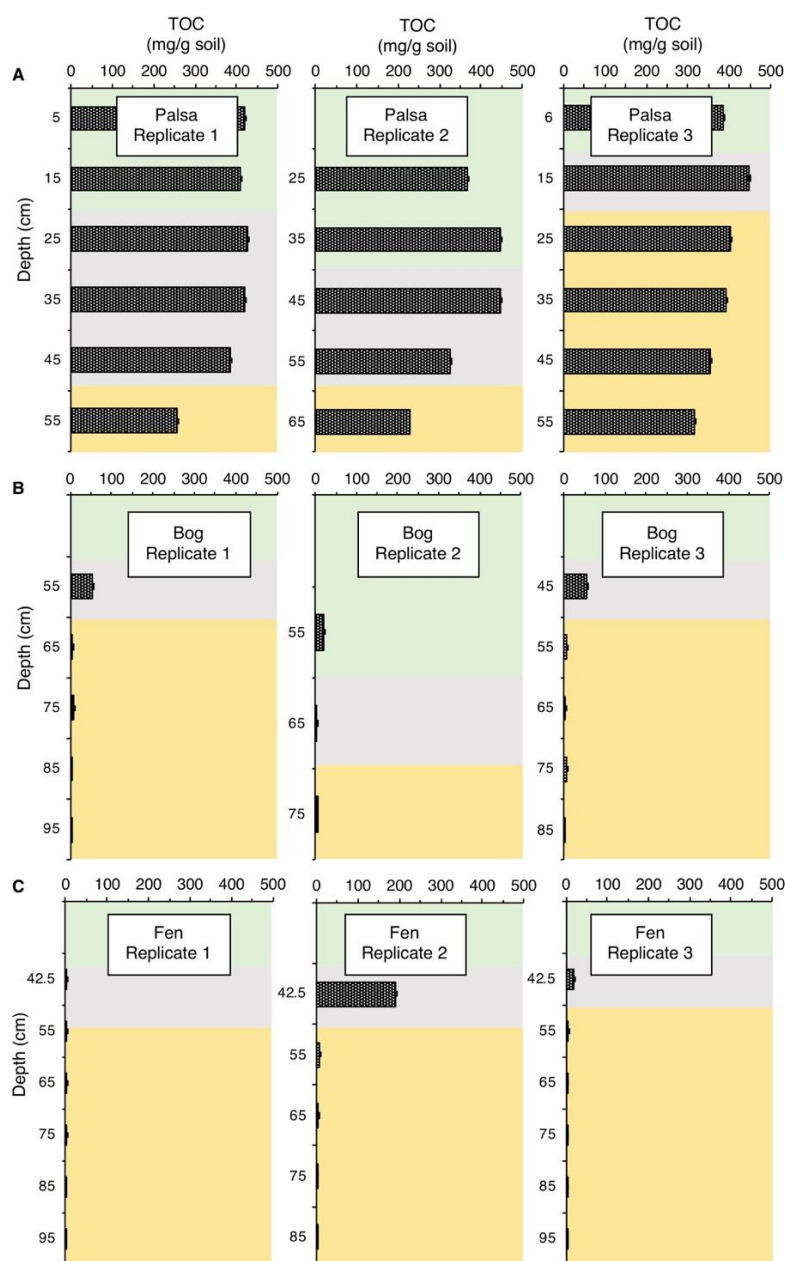
Fig. S4. TOC of replicate cores taken with a Pürckhauer corer: *(A)* Palsa (68°21'26.56"N, 19° 3'0.19"E), *(B)* Bog (68°21'16.02"N, 19° 2'49.21"E) and *(C)* Fen (68°21'17.16"N, 19° 2'36.29"E). Each core was divided into layers in the field and immediately processed. All replicates represent the active layer in September 2017. The bog and fen soils were waterlogged. The green box marks the organic horizon, grey box the transition zone and yellow box the mineral horizon. TOC was determined via combustion. Errors indicate the range of duplicate analyses of each layer in each thaw stage.

629
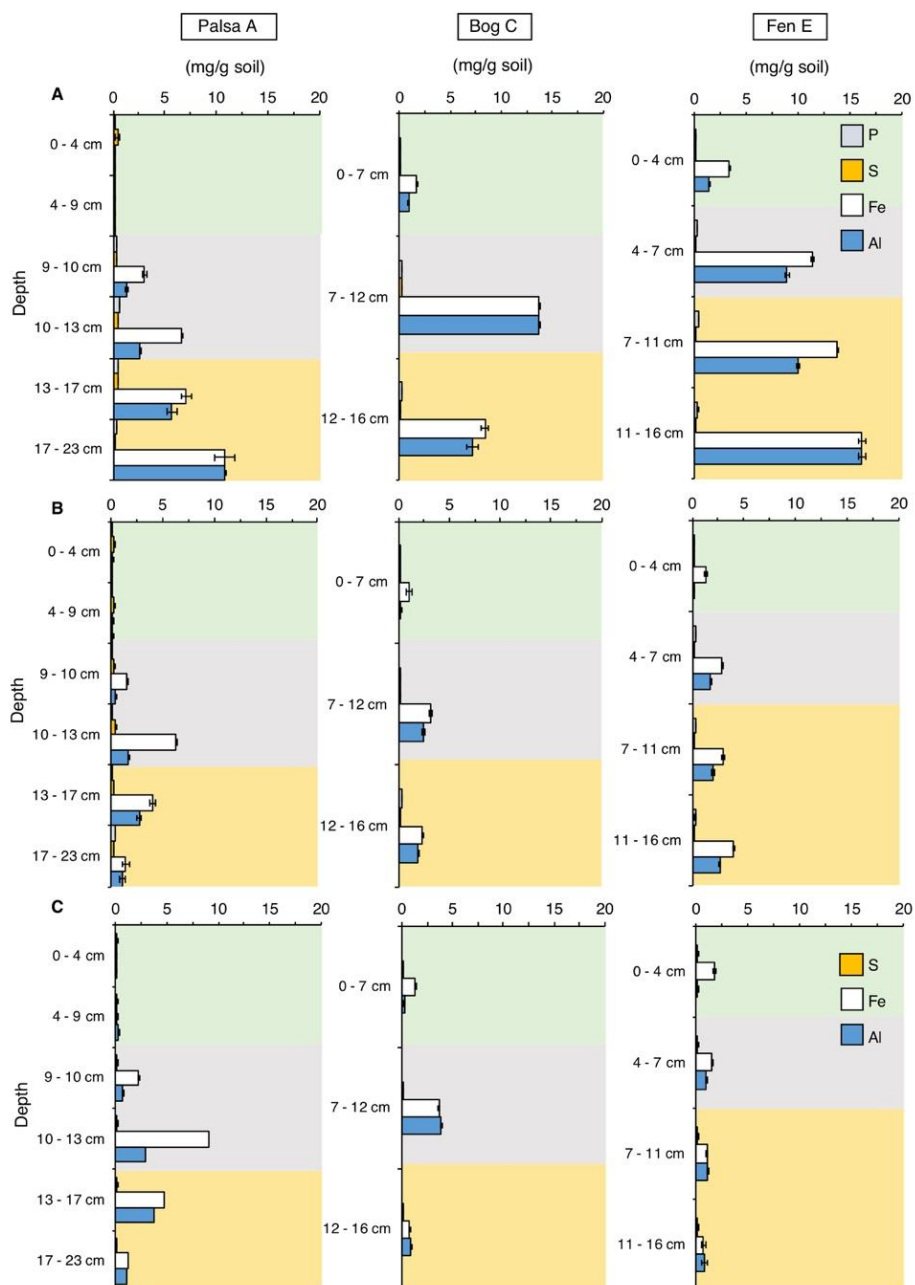
Fig. S5. Other elements (P, S, Fe and Al) in extracts of Palsa A, Bog C and Fen E. *(A)* 6M HCl, *(B)* hydroxylamine-HCl and *(C)* Sodium pyrophosphate extracted. Phosphorous (P) and sulphur (S) concentrations were measured with ICP-MS, whereas iron (Fe) and aluminum (Al) concentrations were analyzed using MP-AES. The green box marks the organic horizon, grey box the transition zone and yellow box the mineral horizon. Errors indicate the range of duplicate analyses of each layer in each thaw stage.

636
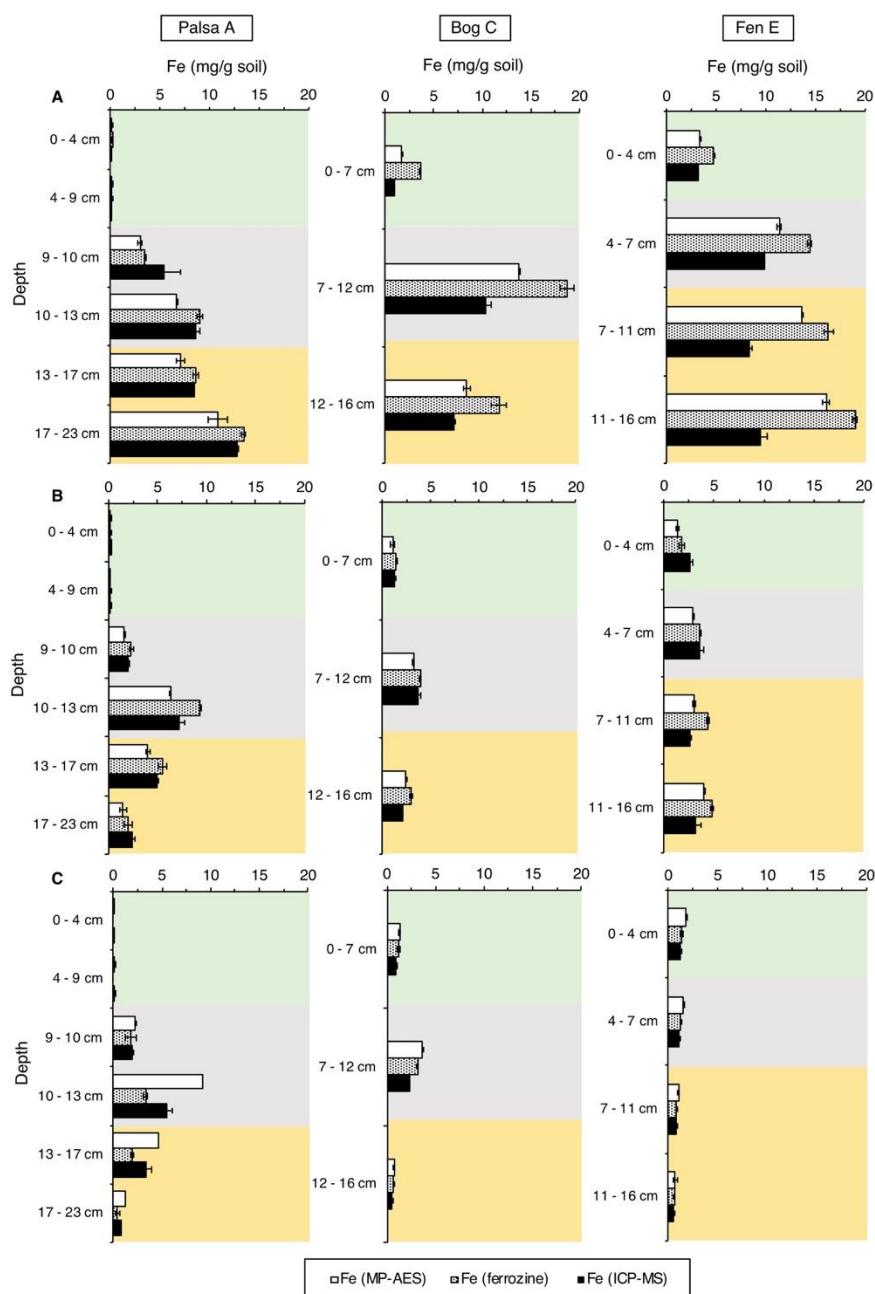
Fig. S6. Fe analysis by MP-AES, ferrozine and ICP-MS analysis. *(A)* 6M HCl extraction. The MP-AES iron values are slightly lower than the ferrozine iron values due to matrix interference during MP-AES measurements of the extracts (HCl). *(B)* Hydroxylamine-HCl extraction. The MP-AES iron values are slightly lower than the ferrozine iron values due to matrix interference during MP-AES measurements of the extracts (HCl). *(C)* Sodium pyrophosphate extraction. The MP-AES values for the sodium pyrophosphate extractable iron are higher than the ferrozine iron values. This could be explained by the dark color of the extracts which disturb the spectrophotometric measurement during ferrozine

644   complexation. After blank subtraction this can result in lower iron concentrations determined by the

645   ferrozine assay.
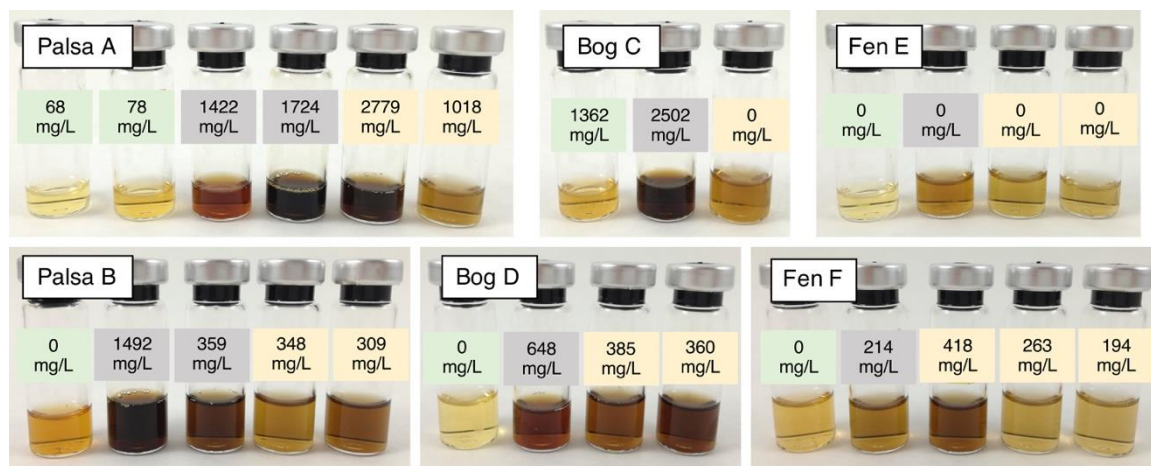
Fig. S7. Extracts of sodium dithionite-citrate extraction. Values indicate the dissolved organic carbon concentrations in the extracts after subtraction of the background of the citrate concentration. The background concentration of the citrate for the analysis of Palsa B, Bog D and Fen F was 20.5±0.14 g/L and for the analysis of Palsa C, Bog E and Fen G was 17.8±0.25 g/L. Pictures of the extracts are shown to highlight the loss of the reactive iron phase and carbon associated with it along the thaw gradient, here visible by brown color loss in the extracts from palsa to fen. Green marks the organic horizon, grey the transition zone and yellow the mineral horizon.

654
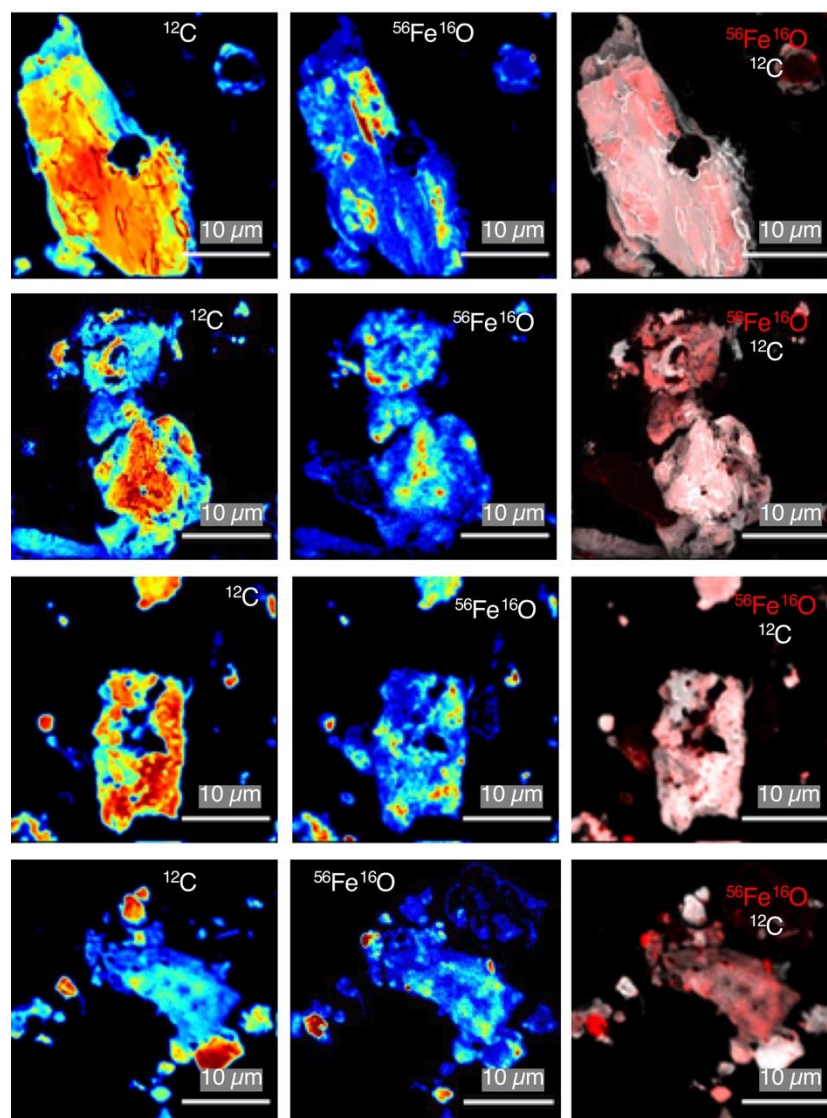
Fig. S8. Four representative particles of the fine fraction of Palsa A analyzed with nanoSIMS showing a close spatial distribution of Fe and C. Seven detectors were used during nanoSIMS measurements for ^{12}C, $^{56}Fe^{16}O$, ^{16}O, $^{12}C^{14}N$, ^{31}P, ^{32}S and $^{27}Al^{16}O$. ^{12}C and $^{56}Fe^{16}O$ are shown for four representative fine particles plus ^{12}C and $^{56}Fe^{16}O$ distributions, overlain in a single image on the left.

659
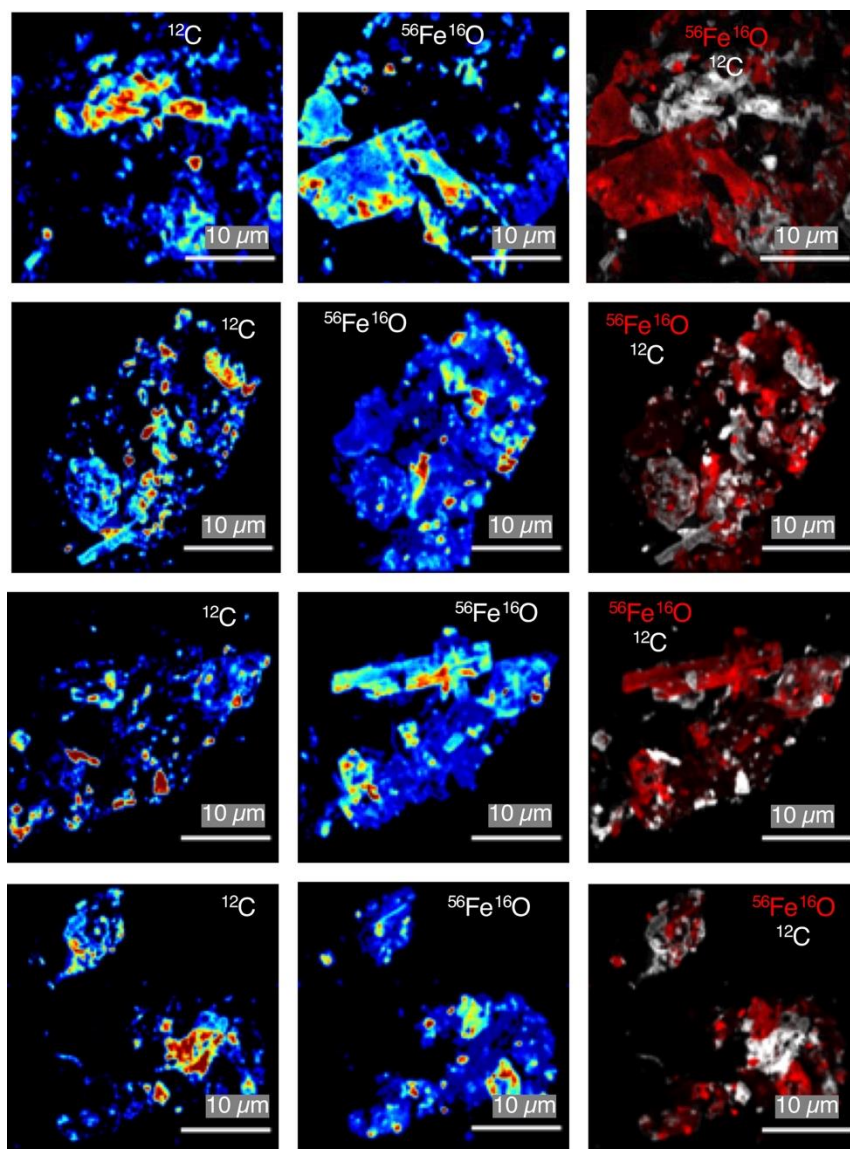
Fig. S9. Four representative particles of the fine fraction of Fen E analyzed with nanoSIMS showing organic-free iron minerals. Seven detectors were used during nanoSIMS measurements for ^{12}C, $^{56}Fe^{16}O$, ^{16}O, $^{12}C^{14}N$, ^{31}P, ^{32}S and $^{27}Al^{16}O$. ^{12}C and $^{56}Fe^{16}O$ are shown for four representative fine particles plus ^{12}C and $^{56}Fe^{16}O$ distributions, overlain in a single image on the left.

664

665 **Table S1.** Absolute and % values of iron and carbon in Palsa B, Bog D and Fen F. In most of the layers,

666 the maximum molar ratio of organic carbon to iron exceeds 1.0, the maximal sorption capacity of reactive

667 iron oxides for natural organic matter (23). Co-precipitation and/or chelation of organic compounds can

668 generate structures with OC:Fe ratios up to 6 to 10 (23). Errors indicate the range of duplicate analyses

669 of each layer in each thaw stage.

	Reactive iron (control corrected)	Reactive iron of total extractable iron	Control iron	C bound to reactive iron (control corrected)	C bound to reactive iron of the total organic carbon	Control carbon	OC:Fe	Total organic carbon	Total extractable Fe
	mg/g	%	mg/g	mg/g	%	mg/g		mg/g	mg/g
Palsa A									
Organic horizon	0.40 ± 0.11	100.00	0.00 ± 0.00	0.94 ± 0.58	0.22	1.37 ± 0.01	2.35	423 ± 0.00	0.20 ± 0.02
	0.29 ± 0.09	100.00	0.00 ± 0.00	2.16 ± 0.95	0.51	1.65 ± 0.08	7.45	422.91 ± 0.13	0.17 ± 0.00
Transition zone	2.55 ± 0.57	72.86	0.29 ± 0.08	30.99 ± 0.71	9.93	3.13 ± 0.02	12.15	312.11 ± 0.33	3.51 ± 0.08
	8.44 ± 0.21	93.86	0.75 ± 0.11	52.50 ± 0.13	14.80	10.36 ± 0.50	6.22	354.72 ± 0.04	8.99 ± 0.28
Mineral horizon	3.17 ± 0.19	36.58	0.25 ± 0.03	27.39 ± 1.61	20.13	2.88 ± 0.08	8.64	136.11 ± 0.21	8.65 ± 0.28
	1.35 ± 0.21	10.00	0.07 ± 0.06	13.58 ± 0.42	18.67	1.39 ± 0.10	10.06	72.71 ± 0.29	13.48 ± 0.22
Bog C									
Organic horizon	1.48 ± 0.18	40.60	0.73 ± 0.07	16.16 ± 3.91	4.85	3.16 ± 1.67	10.92	333.31 ± 0.05	3.63 ± 0.05
Transition zone	2.08 ± 0.05	11.14	0.41 ± 0.04	22.67 ± 8.60	39.42	1.18 ± 0.21	10.90	57.51 ± 0.38	18.65 ± 0.70
Mineral horizon	0.88 ± 0.06	7.52	0.28 ± 0.04	0.00 ± 0.00	0.00	1.04 ± 0.01	0.00	8.28 ± 0.25	11.69 ± 0.81
Fen E									
Organic horizon	2.03 ± 0.14	43.39	0.75 ± 0.00	0.00 ± 0.00	0.00	1.53 ± 0.00	0.00	234.70 ± 0.83	4.68 ± 0.01
Transition zone	2.64 ± 0.03	18.29	0.37 ± 0.00	0.00 ± 0.00	0.00	1.38 ± 0.18	0.00	16.24 ± 0.18	14.46 ± 0.22
Mineral horizon	1.75 ± 0.04	10.71	0.15 ± 0.00	0.00 ± 0.00	0.00	2.57 ± 0.76	0.00	3.52 ± 0.05	16.34 ± 0.44
	1.70 ± 0.04	8.95	0.19 ± 0.01	0.00 ± 0.00	0.00	1.13 ± 0.17	0.00	4.99 ± 0.10	19.01 ± 0.25

670